Controllable Synthesis of Defective TiO_2 Nanorods for Efficient Hydrogen Production

Congcong Xing,[a,b,c] Linlin Yang,[b,d] Maria Chiara Spadaro,[e] Yu Zhang,[a,b]* Pablo Guardia,[f] Jordi Arbiol,[e,g] Tianqi Liu,[a] Xiaolei Fan,[a,h] Marcos Ferná ndez-García,[i]* Jordi Llorca,[c]* Andreu Cabot [b,g]**

[a] Institute of Wenzhou, Zhejiang University, 325006 Wenzhou, China

[b] Catalonia Institute for Energy Research (IREC), Sant Adrià de Besòs, 08930 Barcelona, Spain

[c] Institute of Energy Technologies, Department of Chemical Engineering and Barcelona Research Center in Multiscale Science and Engineering, Universitat Politècnica de Catalunya, EEBE, 08019 Barcelona, Spain

[d] Universitat de Barcelona, 08028 Barcelona, Catalonia, Spain

[e] Catalan Institute of Nanoscience and Nanotechnology (ICN2), CSIC and BIST, Campus UAB, Bellaterra, 08193 Barcelona, Catalonia, Spain

[f] The Institute of Materials Science of Barcelona (ICMAB-CSIC), 08193 Bellaterra, Barcelona, Spain

[g] ICREA, Pg. Lluis Companys 23, 08010 Barcelona, Spain

[h] Department of Chemical Engineering, School of Engineering, The University of Manchester, Oxford Road, Manchester M13 9PL, United Kingdom

[i] Instituto de Catálisis y Petroleoquímica, CSIC. C/ Marie Curie, 2, 28049 Madrid, Spain

* E-mails: CCX: antheaxingcc@gmail.com; YZ: yvz5897@psu.edu; MF-G: mfg@icp.csic.es; JL: jordi.llorca@upc.edu; AC: acabot@irec.cat

ABSTRACT: Nanorods (NRs), with their high atomic surface exposure within a crystalline architecture, facilitate effective diffusion/transport of charge, rendering them particularly suitable for applications requiring both interaction with the media and charge transfer. In this study, we present a straightforward approach to produce brookite-phase titanium dioxide (TiO_2) NRs with tunable defects and narrow size distributions by utilizing methylamine hydrochloride and 1,2-hexadecanediol as shape-directing agents. The presence of Ti^{3+} defect was confirmed by electron paramagnetic resonance and X-ray photoelectron spectroscopy, and its effect on the photocatalytic properties of TiO_2, with and without Pt loading, show that the longest TiO_2 NRs provide the highest photocatalytic and photoelectrochemical hydrogen production activity. Transient photocurrent response analysis, electrochemical impedance spectroscopy, and Mott-Schottky analysis plots indicate that an increase in temperature significantly reduces the interface barrier and lowers the transport resistance, leading to a 104% improvement in hydrogen production rates from 25 °C to 60 °C for the longest TiO_2 NRs. This study underscores the critical role of TiO_2 nanorod dimensions (18-45 nm) in elevating hydrogen production efficiency. At 25 °C, rates surged from 1.6 to 2.6 $mmol \cdot g^{-1}h^{-1}$, and at 60 °C, soared from 3.3 to 5.3 $mmol \cdot g^{-1}h^{-1}$, demonstrating the substantial impact of TiO_2 NRs on enhancing hydrogen generation.

KEYWORDS: TiO_2 nanorod; Photocatalysis; Hydrogen Production; Brookite; Defect

1. INTRODUCTION

Hydrogen stands out as an environmentally favorable energy carrier, offering immense potential for clean energy applications. Nonetheless, realizing its promise hinges on advancing clean production methods to rival conventional fossil fuel-based processes. A promising avenue towards achieving this is harnessing solar energy for water splitting or dehydrogenating organic waste and biomass-derived materials. However, to make this approach economically viable, significant advancements in photocatalytic materials are indispensable. Optimal photocatalysts for hydrogen production necessitate precise electronic structures, characterized by appropriate band gaps and band edges.[1] Moreover, the configuration of surface facets, elemental composition, and overall particle morphology play pivotal roles in facilitating efficient charge transfer and minimizing electron-hole recombination, thereby dictating the overall photocatalytic efficacy.[2]

Drawing upon decades of research since the groundbreaking work of Fujishima and Honda,[3] it is evident that TiO_2 remains unparalleled in its effectiveness for cost-efficient and environmentally friendly photocatalytic water splitting. This enduring superiority stems from a constellation of exceptional attributes intrinsic to TiO_2: its remarkable optoelectronic properties, abundant availability, affordability, non-toxic nature, robust chemical and thermal stability, straightforward synthesis protocols, potent oxidizing capabilities, elevated refractive index, and substantial dielectric constant.[4] Furthermore, TiO_2 emerges as a quintessential n-type wide band gap semiconductor, manifesting in three distinct crystalline phases. Its versatility extends far beyond photocatalytic water splitting, finding widespread utilization across diverse technological domains. From solar cells[5,6] to environmental remediation,[7] electrochromic smart windows,[8] and photocatalysis,[9] TiO_2 serves as a cornerstone material underpinning innovation and advancement.

Leveraging the modulation of polyhedral TiO_2 morphology to enhance the activity of catalytic facets stands as a pivotal strategy in advancing photocatalytic efficiency. Over time, a plethora of TiO_2 designs have emerged and undergone rigorous testing for various photocatalytic reactions, encompassing nanotubes,[10-12] nanosheets,[13,14] hollow spheres,[15] and hierarchically porous structures.[16,17] Among these, TiO_2 NRs emerge as a frontrunner, boasting several inherent advantages in interactions with the surrounding medium, charge transport dynamics, and mechanical resilience[18,19], thereby amplifying performance across photocatalytic, photoelectrochemical, photovoltaic, and gas sensing applications, among others. The capability to finely tune the geometric parameters of TiO_2 NRs, including thickness dictating surface area and length influencing the mean free path of charge carriers, remains highly coveted. Diverse methodologies have been explored to fabricate TiO_2 NRs, ranging from chemical vapor deposition[20-22] and hydrothermal techniques[23-26] to sol-gel[27-29] and colloidal synthesis.[30,31] Among these methods, colloidal synthesis has emerged as particularly effective in achieving precise control over the geometry and dimensions of various material systems, including TiO_2.

Several seminal studies have underscored the profound impact of aspect ratio on the photocatalytic performance of TiO_2 NRs synthesized through colloidal approaches.[32,33] Cozzoli et al. demonstrated precise control over the growth of high aspect ratio anatase TiO_2 NRs via the hydrolysis of titanium tetraisopropoxide (TTIP) in oleic acid (OAc) surfactant, even at a low temperature of 80 °C.[34] Yun et al. elucidated how the aspect ratio of TiO_2 NRs directly influences their photocatalytic decomposition efficiency.[35] An et al. employed hydrothermal synthesis to

manipulate the aspect ratio of TiO_2 NRs by adjusting the quantity of titanium precursor in the growth solution.[36] Ohno et al. elucidated the significant influence of polyvinyl alcohol and polyvinyl pyrrolidone additives on the aspect ratios of TiO_2 NRs.[37] Fu et al. achieved size-tunable and well-crystallized rutile TiO_2 NRs through meticulous control of HCl concentration during synthesis.[38] Furthermore, Cargnello et al. demonstrated that the aspect ratio of TiO_2 NRs could be finely tuned by varying the concentration of $TiCl_4$, resulting in enhanced electron-hole separation following light excitation.[39]

Expanding upon the advancements in colloidal synthesis techniques for TiO_2, our research delved into a mechanistic exploration of brookite-phase TiO_2 NRs synthesis, aiming to achieve precise control over length and narrow size distributions. Leveraging methylamine hydrochloride (MAC) and 1,2-hexanediol (HDDOL) as shape-directing agents, we successfully attained a wide range of size tunability. Employing these tailored TiO_2 NRs, we systematically investigated the influence of NR aspect ratio and reaction temperature on photocatalytic hydrogen production from a bioethanol solution. In a bid to further enhance photocatalytic activity, we introduced platinum (Pt) nanoparticles as a cocatalyst, strategically loaded onto the surface of the TiO_2 NRs. Our study underscores the critical importance of optimizing NR length and reaction temperature to achieve maximal efficiency in hydrogen production within TiO_2 NR-based photocatalytic systems.

2. RESULTS AND DISCUSSION

2.1. Colloidal Synthesis of TiO_2 Nanorods

TiO_2 NRs were synthesized using an organic solution colloidal hydrolysis method, as detailed in the experimental section. Briefly, titania nuclei formation occurred in the presence of oleylamine (OAm), 1-octadecanol (ODO), OAc, and subsequently, either 1,2-HDDOL or MAC, by heating a titanium (IV) chloride ($TiCl_4$) precursor stock solution to 290 °C (refer to Figure S1). At this moderate temperature, OAm and OAc slowly react, generating small amounts of water, thereby facilitating the gradual hydrolysis and condensation of $TiCl_4$ alongside the release of HCl.[40] Following nucleation, TiO_2 NRs were further elongated by the gradual addition of additional $TiCl_4$ stock solution into the initial nuclei solution maintained at 290 °C. This two-step synthesis method effectively prevents the formation of additional NRs during the growth of pre-existing ones. OAm and OAc serve a dual role as coordinating/stabilizing solvents and sources of water, while chloride

ions play a crucial role in directing the asymmetric growth of TiO_2 and determining its aspect ratio (**Figure** 1a).

The resulting materials exhibited elongated structures with a width of approximately 2.5 ± 0.7 nm and variable lengths, dependent on the specific synthesis conditions employed. We investigated the influence of MAC and 1,2-HDDOL on the surface properties of the nanoparticles to modulate the amount of chlorine binding at the surface. Transmission electron microscopy (TEM) images depicted in **Figures** 1b-d confirmed the effect of MAC and 1,2-HDDOL on the length of the TiO_2 NRs. Our hypothesis suggests that the addition of MAC increases the chlorine concentration at the nanoparticle surface, impeding TiO_2 nucleation and resulting in the formation of longer NRs. Conversely, 1,2-HDDOL competes with chloride ions for binding sites on the TiO_2 NR surface, leading to a decrease in surface chlorine concentration and promoting the formation of TiO_2 nuclei, resulting in shorter NRs. Further investigations focused on three types of TiO_2 NRs designated as short (S-TiO_2), medium (M-TiO_2) and long-length (L-TiO_2) NRs with average lengths of 18, 28, and 45 nm, respectively (see Figure S2 and Table S1). Despite the random orientation of TiO_2 NRs relative to the electron beam, they exhibit high crystal quality, as depicted in **Figure** 1e. In the color frequency filtered map, the highly crystalline TiO_2 NRs are observable, with each orientation represented by a distinct color. The orthorhombic brookite TiO_2 phase was confirmed by X-ray diffraction (XRD) patterns of the TiO_2 NRs with varying lengths, as depicted in **Figure** 1g. Additionally, electron energy loss spectroscopy (EELS) spectra, presented in **Figures** 1f and S3,4, verified the presence of the brookite TiO_2 phase across all TiO_2 NRs with different lengths.

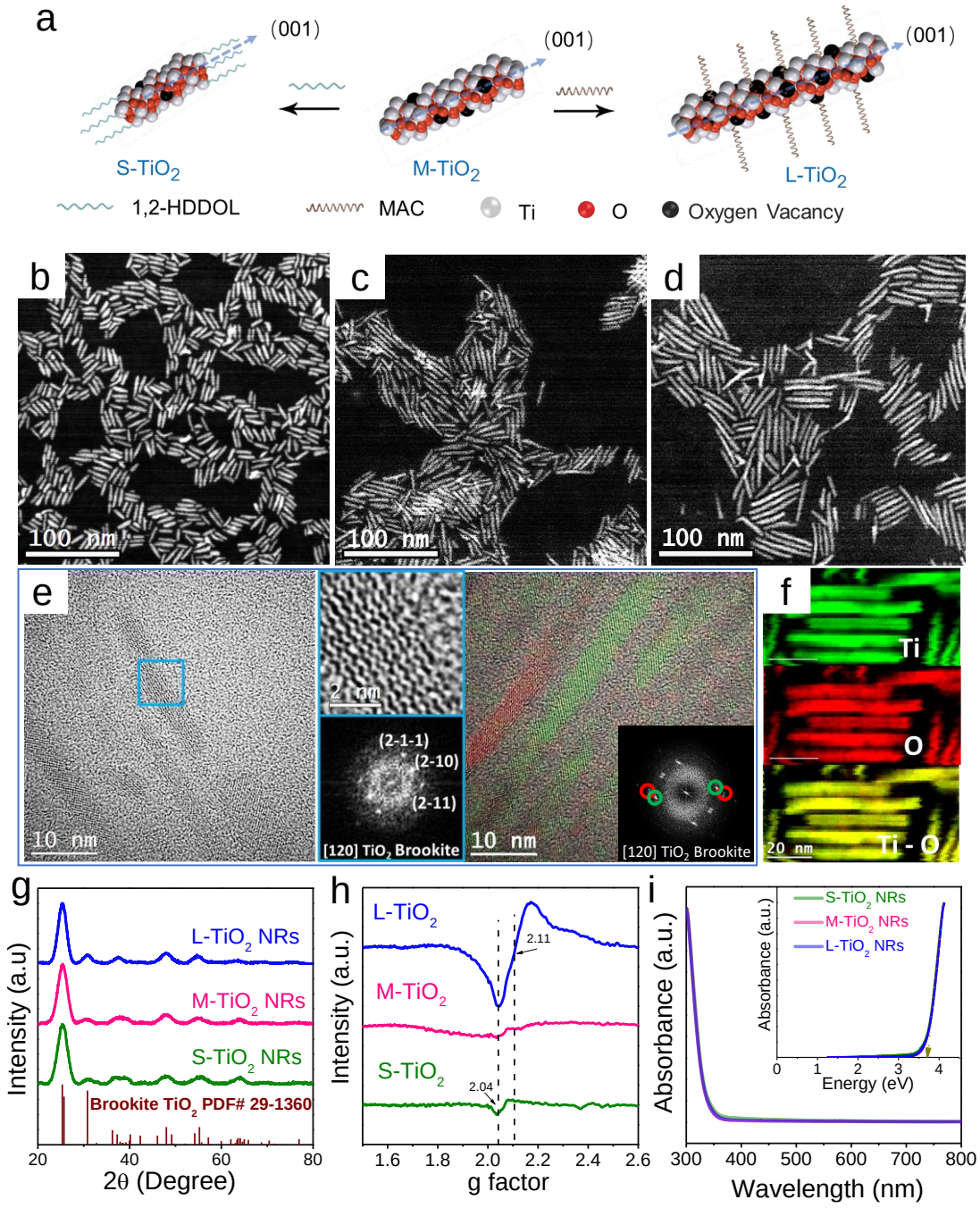

Figure 1. (a) Schematic illustration of the influence of HDDOL and MAC on the size and aspect ratio of the TiO_2 NRs. Representative TEM micrographs (scale bar 100nm) of (b) S-TiO_2, (c) M-TiO_2, and (d) L-TiO_2. HRTEM micrographs of TiO_2 NRs showing the Brookite orthorhombic crystal phase: (e) L-TiO_2 NRs oriented along the [120] zone axis, and TiO_2 NRs where each orientation appears with different color (green and red). (f) EELS chemical composition maps of

L-TiO_2 NRs: Ti L edge at 456 eV (green) and O K edge at 532 eV (red). (g) powder XRD pattern of S, M, L-TiO_2 NRs, including reference pattern for TiO_2 (PDF# 29-1360). TiO_2 nanostructures with rod regular shape show TiO_2 Brookite Orthorombic crystal phase. (h) EPR spectra of S, M, L-TiO_2 NRs after ligand exchange. (i) UV-vis spectra of S, M, L-TiO_2 NRs, including the band gap inside.

Electron paramagnetic resonance (EPR) spectroscopy was utilized to probe the presence of unpaired electron spins within TiO_2 NRs of varying lengths. In **Figure** 1h, EPR resonance signals were recorded at T = 77 K for S, M, and L- TiO_2 NRs. While previous studies have attributed EPR signals at a g-value of 2.11 to electrons trapped at oxygen vacancies on the surface,[41,42] indicating the presence of Ti^{3+} species within our TiO_2 NR samples.[43,44] Remarkably, the L-TiO_2 NRs exhibited a notably stronger EPR signal, suggesting a substantially elevated concentration of Ti^{3+} species attributed to their increased length. Consequently, it can be inferred that defects within the L-TiO_2 NRs primarily manifest as Ti^{3+} rather than oxygen vacancies.

X-ray photoelectron spectroscopy (XPS) analyses were conducted to investigate the chemical composition and oxidation states of titanium atoms on the surface of TiO_2 NRs. The binding energies were calibrated using the C 1s peak at 284.8 eV as the reference. The XPS survey and high-resolution spectra of Ti 2p and O 1s from TiO_2 NRs are shown in Figure S5a-c. The comprehensive XPS survey confirms that the TiO_2 NRs predominantly consist of titanium and oxygen. Notably, the ratios of Ti^{3+} 2p3/2 to Ti^{4+} 2p3/2 for L-TiO_2, M-TiO_2, and S-TiO_2 are 0.113, 0.105, and 0.077, respectively. A higher Ti^{3+} 2p3/2 to Ti^{4+} 2p3/2 ratio indicates increased defect density.[45] Additionally, a positive shift of 0.3 eV in the O 1s spectrum was observed for L-TiO_2 compared to S-TiO_2 and M-TiO_2 NRs. The positive shifts in both Ti 2p and O 1s spectra suggest the existence of abundant defects, which are capable of raising the Fermi level.[46] The incorporation of Ti^{3+} into TiO_2 has been demonstrated as an effective strategy to enhance the visible light response and improve the photocatalytic properties of TiO_2-based photocatalysts. This work, however, will elucidate that the incorporation of Ti^{3+} into TiO_2 also serves as an innovative approach to enhance the photocatalytic properties of TiO_2-based photocatalysts under UV light irradiation.

To eliminate loosely bonded ligands from the surface of TiO_2 NRs, we employed a hexane NH_4SCN solution to suspend the NRs. Subsequently, ethanol was introduced to create a two-phase

mixture, as outlined in the experimental section. Upon agitation, the TiO_2 NRs migrated from the weakly polar hexane phase to the polar ethanol phase, effectively shedding the surfactant molecules. This phenomenon was corroborated by infrared (IR) spectroscopy, as depicted in Figure S6. The peaks observed in the IR spectra before ligand removal, such as those at 1066 cm^{-1} (C-O), 1150 cm^{-1} (C-N), 1458 cm^{-1} (CH2), 1582 cm^{-1} (C=C), 2850 cm^{-1} and 2930 cm^{-1} (C-H), corresponded to functional groups associated with the ligands bound to the TiO_2 NRs. Following ligand removal, these functional groups disappeared from the TiO_2 NR surfaces. Additionally, the IR spectra revealed the presence of abundant hydroxyl groups (-OH) on the TiO_2 NR surfaces post-removal, contributing to increased hydrophilicity and water absorptivity.[47]

Ultraviolet-visible (UV-Vis) spectra revealed that the absorption of light due to band-to-band electronic transitions remained unaffected by the aspect ratio of the TiO_2 NRs, indicative of an optical band gap energy (Eg) of approximately 3.4 eV. This value aligns with previous studies,[39] which have demonstrated that Eg values are strongly influenced by sample crystallinity, synthesis method, and product morphology (**Figure** 1i).[48,49]

2.2. Photocatalytic activity

While photocatalytic water splitting is strongly limited by the sluggish reaction kinetics of the oxygen evolution reaction, the direct use of solar light to extract hydrogen from organic waste or biomass-derived products such as bioethanol is an excellent alternative. The use of organic molecules as a hydrogen source offers a less energy-demanding oxidation reaction. For instance, the Gibbs free energy for the dehydrogenation of ethanol to acetaldehyde (C_2H_5OH (g) → CH_3CHO (g) + H_2; 41.5 kJ mol^{-1})[50] is significantly lower than that of H_2 evolution from water (H_2O (g) → H_2 + ½O_2; 237 kJ mol^{-1}).[51,52] Besides, the easier oxidation of ethanol strongly reduces the recombination of electron-hole pairs, thus increasing the quantum efficiency. An additional advantage of the production of hydrogen from the reforming of organic waste or biomass-derived organics is the potential co-generation of valuable organic chemicals.

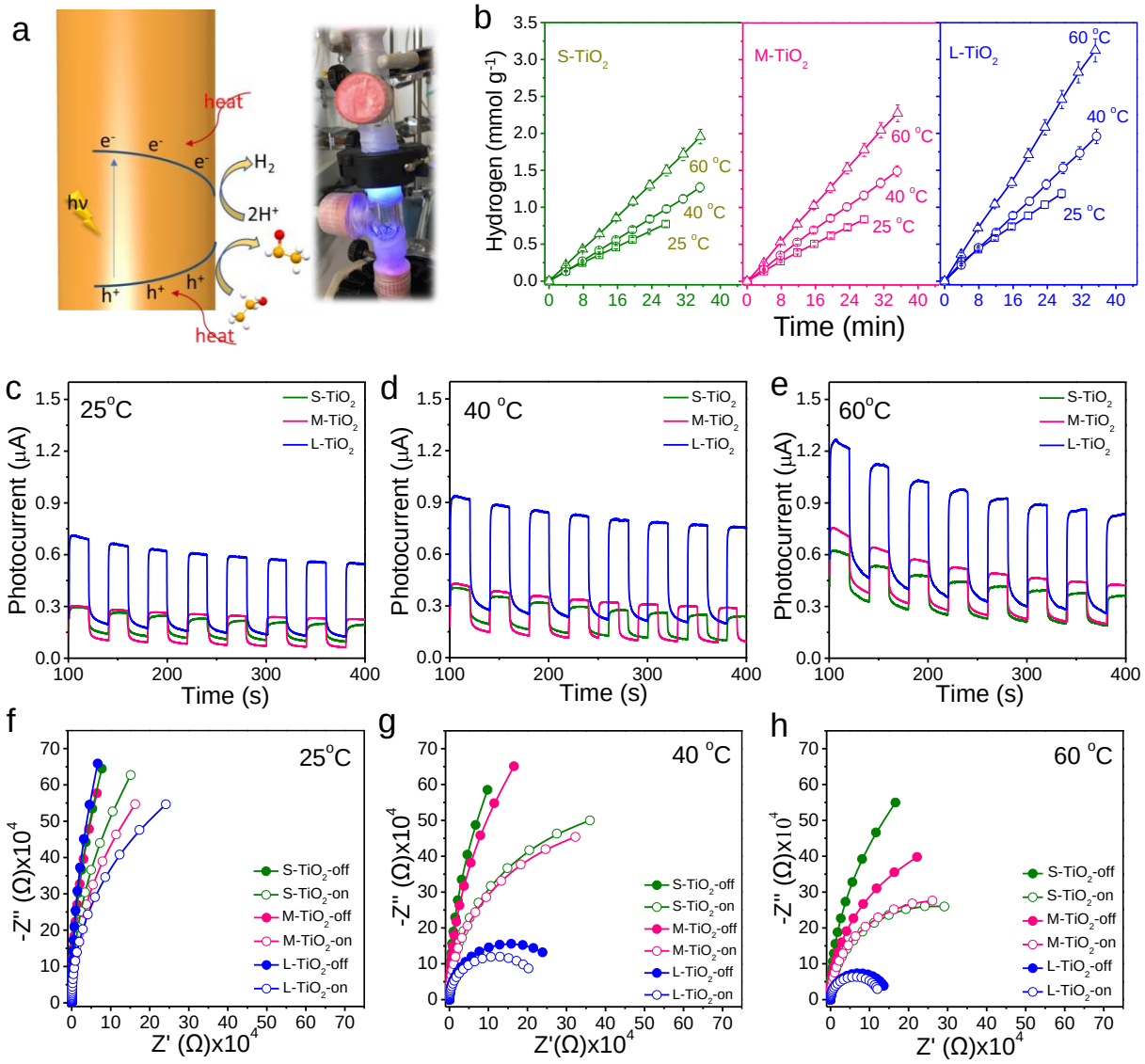

Figure 2. (a) Schematic illustration of the TiO_2 according to photothermal according to photo catalytic mechanism and photocatalytic reactor. (b) Photocatalytic H_2 production of S, M, L-TiO_2 NRs under UV light irradiation (365 ±5 nm, 79.1±0.5 mW·cm^{-2}) at different temperature. The transient photocurrent responses of (c) S-TiO_2, (d) M-TiO_2, and (e) S-TiO_2 NRs at 0.6 V vs. RHE. EIS fit curve at 0.05 V vs. RHE of (f) S-TiO_2, (g) M-TiO_2, and (h) S-TiO_2 NRs in 0.5 M Na_2SO_4 aqueous solution with and without visible light (AM 1.5G light source radiation intensity: 100 mW·cm^{-2}).

Figure 2b illustrates the photocatalytic activity of TiO_2 NRs in hydrogen (H_2) production from a water-ethanol mixture (9:1, molar) under Hg lamp irradiation (λ =365 nm, **Figure** 2a).

impact of temperature was examined by evaluating the photocatalytic activity at 25 °C, 40 °C, and 60 °C. In all cases, the photoreaction yielded hydrogen and acetaldehyde exclusively in equimolar amounts, indicating that ethanol dehydrogenation was the sole source of hydrogen. At ambient temperature (25 °C), the L-TiO_2 NRs exhibited the highest H_2 production rate and apparent quantum efficiency (AQY) at 2.6 mmol·$g^{-1}$$h^{-1}$ and 0.7%, respectively. These values surpassed those obtained for M-TiO_2 and S-TiO_2 NRs, which achieved 1.8 mmol·$g^{-1}$$h^{-1}$ and 0.49%, and 1.6 mmol·$g^{-1}$$h^{-1}$ and 0.43%, respectively. The photocatalytic activity substantially increased with temperature for all materials. Upon raising the temperature, both the H_2 production rate of long TiO_2 NRs increased to 3.3 mmol·$g^{-1}$$h^{-1}$ at 40 °C, and further to 5.3 mmol·$h^{-1}$$g^{-1}$ at 60 °C. In comparison, the H_2 production rate of M-TiO_2 and S-TiO_2 NRs were 2.5 and 2.2 mmol·$g^{-1}$$h^{-1}$ at 40 °C, 3.8 and 3.3 mmol·$g^{-1}$$h^{-1}$ at 60 °C, respectively (see Figure S7). Consequently, as the temperature increased from 25 °C to 60 °C, the H_2 production rate of S-TiO_2, M-TiO_2, and L-TiO_2 was enhanced by 106%, 111%, and 104%, respectively. This significant temperature effect may be attributed to the promotion of acetaldehyde desorption from the TiO_2 surface, thereby unblocking surface active sites.[53]

2.3. Photocatalytic Mechanism

To gain additional insight into the photocatalytic process, we measured the transient photocurrent (TPC) response of the TiO_2 NRs with different lengths. As displayed in **Figures** 2c-e, we observed an increase in the steady-state photocurrent with the length of the TiO_2 NRs. Upon illumination at room temperature (25 °C), the current densities for S, M, and L-TiO_2 NRs increased by approximately 100%, 243%, and 300%, respectively, compared to the dark conditions. We hypothesize that this experimental result can be attributed to a more effective suppression of surface charge recombination when increasing the NR length, which is associated with the delocalization of the charge carriers and/or an improvement of the charge transport properties with the increase of the NR size. We observed that while the current density increased with temperature due to an increase in the charge carrier concentration within the TiO_2 semiconductor, the relative photocurrent, i.e., the current density increases upon illumination, decreased. This result can be explained by the lower relative weight of the generated photocarriers.

The Nyquist plots and fitting parameters of the EIS spectra obtained from the different materials in dark and under irradiation are displayed in **Figures** 2f-h and Table S2-S4, respectively.

As expected, the L-TiO_2 NRs are characterized by the smallest impedances. Besides, impedances strongly decreased when increasing temperature, as it corresponds to a non-degenerated semiconductor associated with an increase of the free carrier density.

M-S plots were collected to determine the sign of the majority carriers and the flat band positions (E_{fb}) of TiO_2 NRs (Figures S8-S11). All M-S plots showed positive slopes, confirming the n-type conductivity of the TiO_2 NRs. E_{fb} values negatively shifted upon light irradiation, implying a stronger band bending, pointing at the accumulation of photogenerated electrons at the surface of TiO_2 NRs. That is, an n^+/n TiO_2 homojunction is generated increasing the free carrier concentration at the TiO_2 surface available for photocatalytic H_2 generation.[54-56] At ambient temperature, larger E_{fb} differences upon light irradiation were obtained when increasing the NRs length, being the L-TiO_2 NRs, the ones showing the largest E_{fb} change thus the more efficient separation of photogenerated charge carriers. When increasing temperature, the E_{fb} differences become less obvious. Although the surface area decreased with the elongation of the nanorods, from 129.52 m^2/g for S-TiO_2 to 60.16 m^2/g for L-TiO_2 (Figure S12), the markedly higher photocatalytic performance observed in L-TiO_2 indicates that the formation of Ti^{3+} defects play a crucial role that significantly enhance the charge carrier concentration and promote improved charge separation, thereby boosting the photocatalytic efficiency.

2.4. Photocatalytic Performance of Pt-TiO_2

To enhance the photocatalytic efficiency of TiO_2 NRs for hydrogen photoproduction, Pt was incorporated on the surface of TiO_2 NRs via photoreduction of H_2PtCl_6, as described in the Experimental section. The presence of Pt nanoparticles on the TiO_2 NR surface was confirmed by XRD, TEM imaging and energy dispersive spectroscopy (EDS) analysis, which showed the dispersed black spots corresponding to about 5 nm Pt nanoparticles and the amount of Pt loaded to be about 1 wt%, respectively (Figures S13a-c, and Table S5). The incorporation of Pt significantly increased the H_2 photoproduction rate by up to a factor of 20 at 60 °C, as shown in **Figures** 3a, c. However, the highest H_2 production rate and AQY were obtained with the longest TiO_2 NRs, at 81 $mmol \cdot g^{-1} \cdot h^{-1}$ and 22%, respectively (Figures S14 and S15). The incorporation of Pt could be correlated with a more effective delocalization of electrons along the NR, leading to a more efficient electron-hole separation and carrier extraction at Pt sites.

The high photocatalytic activity of Pt-loaded TiO_2 NRs was demonstrated by comparison with literature benchmark materials in Table S5. As the temperature increased, the H_2 production rate of Pt-TiO_2 NRs also increased, but more moderately than in the case of bare TiO_2 NRs. As the temperature increased from 25 to 60 °C, the H_2 production rate of Pt-S-TiO_2, Pt-M-TiO_2, and Pt-L-TiO_2 changed by -0.3%, 32%, and 16%, respectively (Figure S15).

According to the results of linear sweep voltammetry (LSV) (Figure S16a), the Pt-TiO_2 heterojunction exhibits an obvious photocurrent enhancement with increasing bias potential as compared with the pure TiO_2, which demonstrates that the photoinduced electron–hole recombination is hindered to accelerate electron transfer. As a result, the introduction of Pt significantly increased the current densities measured, also increased the photocurrent response, as shown in Figure S16b.

The Arrhenius plot in Figure S17 shows that the hydrogen production rate over S, M, L-TiO_2 and Pt-TiO_2 NRs exhibited similar apparent activation energies (E_a) of about 15 $kJ \cdot mol^{-1}$ in the temperature range tested.[57] However, the Pt-TiO_2 NRs exhibited even lower E_a compared to TiO_2 NRs.

The conduction band edge of TiO_2 typically resides at approximately -0.468 eV vs. NHE, while the valence band edge is situated around +2.932 eV vs. NHE (further elaborated in the Supporting Information).[52] The Fermi level of Pt is approximately +0.8 eV vs. NHE, and the redox potential of ethanol (C_2H_5OH/CH_3CHO) is approximately -0.197 eV vs. NHE.[58] By clearly delineating these energy levels, we gain a better understanding of the alignment and dynamics of electron and hole transfer, thereby validating the proposed mechanism for photocatalytic hydrogen production.

The photocatalytic H_2 production on Pt-TiO_2 catalyst involves four key steps, including photon irradiation, photocarrier generation, carrier separation, reduction and oxidation. (**Figure** 3b) Initially, TiO_2 absorbs photons with energy equal to or greater than its bandgap, prompting the excitation of electrons from the valence band (VB) to the conduction band (CB), thereby generating electron-hole pairs. Owing to the presence of abundant electron and hole traps (Ti^{3+} defects) at the surface of TiO_2, which favored the electron transfer to adsorbates during the catalytic process. Subsequently, the photogenerated electrons in the CB of TiO_2, situated at -0.468 eV vs. NHE, are transferred to Pt nanoparticles, serving as co-catalysts. This separation of carriers

has greatly suppressed recombination of the photogenerated electron-hole pairs, which in turn increased the lifetime of the charge carries of L-TiO_2 compared to that of S-TiO_2 thus promising an efficient catalyst for subsequent H_2 reduction. The electrons on Pt then participate in the reduction of protons to hydrogen gas, a process bolstered by Pt's high work function and conductivity. Concurrently, the holes in the VB of TiO_2, positioned at +2.932 eV vs. NHE, oxidize C_2H_5OH to acetaldehyde CH_3CHO with a redox potential of -0.197 eV vs. NHE, thereby providing the protons requisite for hydrogen evolution. The efficient separation and utilization of photogenerated charge carriers-electrons for hydrogen evolution and holes for ethanol oxidation-ensures a continuous and effective photocatalytic process.

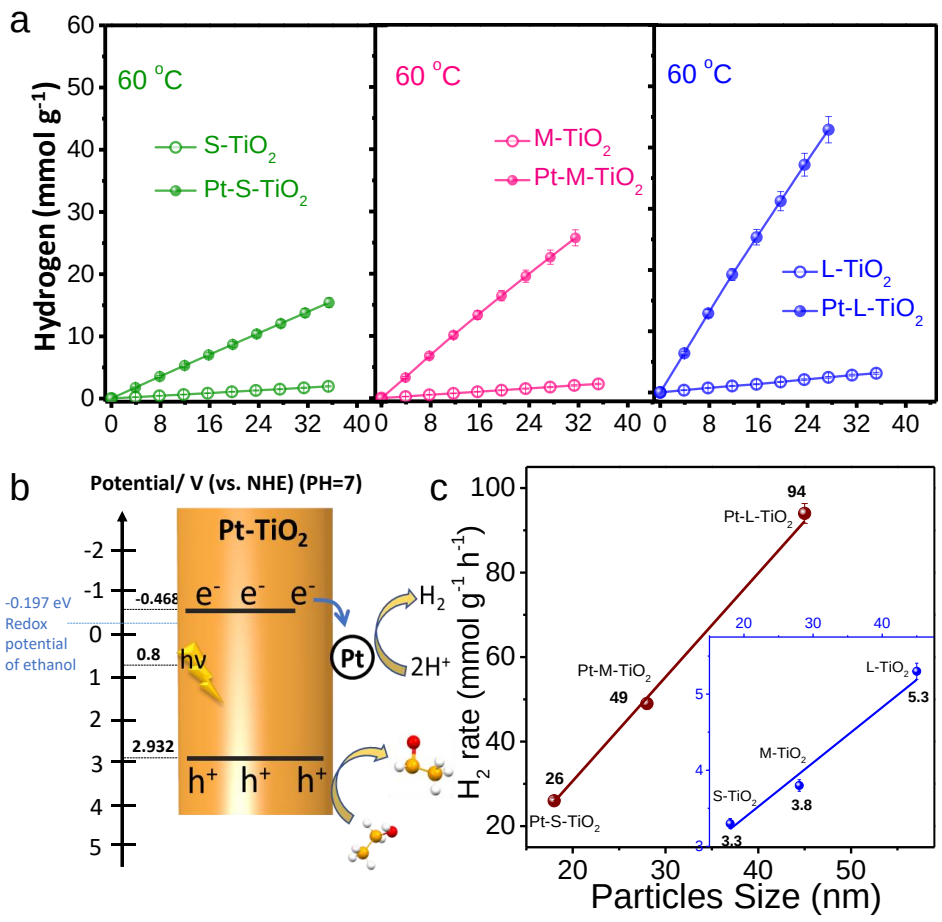

Figure 3. (a) Photocatalytic H_2 production of S, M, L-TiO_2 NRs and Pt-S, M, L-TiO_2 NRs under UV light irradiation (365 ± 5 nm, 79.1±0.5 mW·cm^{-2}) at 60 °C. (b) Schematics of the electronic

band structures of Pt-L-TiO_2. (c) Highest H_2 production rate obtained from (a) with different length of NRs.

3. CONCLUSION

In summary, we synthesized colloidal brookite-phase TiO_2 NRs with tunable defects and investigated their photocatalytic properties for H_2 production. The NR defects was controlled by adjusting the nucleation events using MAC or 1,2-HDDOL. We established the correlation between the photocatalytic H_2 evolution rate with the NR length, which shows that the longest NRs exhibited the highest activities with the H_2 production rate and AQY at 2.6 $mmol \cdot g^{-1}h^{-1}$ and 0.7%, respectively, under ambient conditions. Increasing the temperature resulted in a more than two-fold increase in the H_2 production rate of the longest NRs, up to 5.3 $mmol \cdot h^{-1}g^{-1}$ at 60 °C. Photoelectrochemical characterization revealed a three-fold increase in current densities upon illumination for the longest NRs, indicating effective suppression of surface charge recombination. The delocalization of charge carriers and/or an improvement in charge transport properties may explain this effect. Increasing the temperature increased the current density due to an increase in charge carrier concentration within the TiO_2 semiconductor but decreased the relative photocurrent due to the lower relative weight of the generated photocarriers. Mott-Schottky measurements showed an accumulation of electrons at the TiO_2 surface upon light irradiation, which increased with the NR length and decreased with temperature. The incorporation of Pt as a cocatalyst significantly improved the H_2 photoproduction rate by more than an order of magnitude. The highest H_2 production rate and AQY were obtained with the longest NRs in the presence of Pt, at 81 $mmol \cdot g^{-1}h^{-1}$ and 22%, respectively. In conclusion, our study demonstrates the tunability of NR defects and the significance of temperature in enhancing the photocatalytic H_2 production rate of TiO_2 and Pt-TiO_2 NRs.

4. EXPERIMENTAL SECTION

Preparation of Stock Solutions. Stock solutions were prepared in a glovebox under a nitrogen atmosphere. The $TiCl_4$ stock solution consisted of 0.12 g $TiCl_4$ in 1.5 mL OAc and 3.4 mL ODO. The $TiCl_4$ stock solution was stirred on a hot plate at the temperature of 80 °C to promote the dissolution of $TiCl_4$. Once dissolved, the $TiCl_4$ stock solution turned brown.

Synthesis of TiO_2 NRs. For M-TiO_2 NRs, 15 mL OAm, 5.2 mL ODO, 0.25 mL OAc were degassed in a 100 mL flask at 120 °C for 1 h. After that, the system temperature was allowed to

cool down to 60 °C to add 0.25 mL stock solution. Then, the solution was quickly heated to 290 °C within 15 min and held for 10 min for the formation of seed crystals. Subsequently, an additional 4 mL stock solution was slowly injected with the speed of 0.2 mL·min^{-1} into the flask kept using a New Era Pump Systems NE-1000 syringe pump. The mixture was allowed to react at 290 °C for 5 min before naturally cooling to room temperature. S-TiO_2 and L-TiO_2 NRs were synthesized using the same procedure except for adding 10 mmol of HDDOL or MAC in the initial solution. The obtained TiO_2 NRs were finally collected by precipitation, adding 15 mL hexane, and centrifuging at 5500 rpm for 5 min. The supernatant was discarded and the precipitate was dispersed in 5 mL hexane for further use.

Ligand Removal. The native organic ligands were displaced from the NRs surface using a NH_4SCN solution. Briefly, 1 mL hexane solution containing NRs (5 mg·mL^{-1}) was mixed with 1 mL 0.15 M NH_4SCN solution (in ethanol). The mixture was then shacked for several minutes with a vortex and finally centrifuged at 4000 rpm for 3 min. The resulting product was further washed with 2 mL ethanol twice to remove the residual NH_4SCN.

Photochemical Deposition of Platinum on TiO_2 NRs. Pt was photochemically deposited onto TiO_2 NRs by irradiating a suspension, which consisted of 5 mg TiO_2 NRs and 10 mL ethanol solution (10.0 vol%) containing 1 wt% H_2PtCl_6, using an AM 1.5G solar power system for 4 h.

Materials Characterization. The samples' crystal structures were determined using XRD with a Bruker AXS D8 Advance X-ray diffractometer. SEM (Zeiss Auriga) captured surface morphology, while Oxford EDX combined with the Zeiss Auriga SEM analyzed elemental composition. TiO_2 lattice structure was visualized via high-resolution TEM (FEI Tecnai F20) at 300 keV with 0.18 nm point and 0.11 nm lattice resolution. UV-Vis spectra, obtained with a Shimazu UV-Vis spectrometer, used $BaSO_4$ as background for light absorption analysis. EPR measurements were conducted at 9.39 GHz using a Bruker EMXmicro6/1 spectrometer, over the range of 400-6000.

Photocatalytic Hydrogen Evolution. A cellulose paper loaded with 2.0 mg of photocatalyst was placed within a reactor equipped with UV LEDs (365 ±5 nm) from SACOPA S.A.U. UV light intensity was 79.1 ±0.5 mW·cm^{-2} at the sample, while a saturated Ar stream (20 mL·min^{-1}) with a water:ethanol ratio of 9:1 was used. Online monitoring via Agilent 3000A MicroGC with MS 5 Å, Plot U, and Stabilwax columns occurred every 4 minutes. Before experimentation, the photoreactor was purged with the gaseous reactant mixture for 30 minutes. The UV-visible light

source comprised 372 ±5 nm UV LEDs and visible light LEDs (CCT 6099 K, CRI 74), with light irradiation at 11.2 ±0.5 $mW \cdot cm^{-2}$ for UV light at the sample.

Photoelectrochemical Measurements. A CHI760e instrument was used in a three-electrode cell configuration. The counter electrode was a platinum mesh, and an Ag/AgCl electrode served as the reference electrode. A 0.5 M Na_2SO_4 electrolyte solution was employed. The working electrode was prepared by depositing a photocatalyst onto an ITO glass electrode (1 cm ×1 cm) and heating it at 200 °C for 1 hour. Potentials were referenced to Ag/AgCl and converted to potentials vs. the RHE using the Nernst equation ($E_{RHE} = E_{Ag/AgCl} + 0.059\ pH + 0.196$). TPC and EIS measurements were performed in the dark and under simulated AM1.5G solar irradiation (100 $mW \cdot cm^{-2}$) at ambient temperature. EIS measurements involved applying a sinusoidal AC perturbation of 5 mV over a frequency range of 0.01-100,000 Hz. M-S spectra were obtained by scanning the bias potential from -1.2 to 0.2 V vs. Ag/AgCl at a scan rate of 0.01 $V \cdot s^{-1}$.

ASSOCIATED CONTENT

Supporting Information. Details of the materials, materials characterization, photocatalytic and photoelectrochemical measurements, additional TEM micrographs, EELS chemical compositional maps, size distribution histograms, hydrogen evolution graphs, EDS spectra, M-S graphs, and comparison tables. This material is available via the Internet.

Corresponding Author

* E-mails: CCX: antheaxingcc@gmail.com; YZ: yvz5897@psu.edu; MF-G: mfg@icp.csic.es; JL: jordi.llorca@upc.edu; AC: acabot@irec.cat.

Author Contributions

The manuscript was written through the contributions of all authors. All authors have approved the final version of the manuscript.

Declaration of Competing Interest. There are no conflicts to declare.

ACKNOWLEDGMENT

This work was supported by the European Regional Development Funds and by the Spanish Ministerio de Economía y Competitividad through projects PID2021-124572OB-C31 and

COMBENERGY (PID2019-105490RB-C32). ICN2 acknowledges funding from Generalitat de Catalunya 2021SGR00457. This study was supported by MCIN with funding from European Union NextGenerationEU (PRTR-C17.I1) and Generalitat de Catalunya. This research is part of the CSIC program for the Spanish Recovery, Transformation and Resilience Plan funded by the Recovery and Resilience Facility of the European Union, established by the Regulation (EU) 2020/2094. The authors thank support from the project NANOGEN (PID2020-116093RB-C43), funded by MCIN/AEI/10 .13039/501100011033/ and by "ERDF A way of making Europe", by the "European Union". ICN2 is supported by the Severo Ochoa program from Spanish MCIN/AEI (Grant No.: CEX2021-001214-S) and is funded by the CERCA Programme/Generalitat de Catalunya. P. G. acknowledges financial support from the Spanish government (MICIU) through the Ramon y Cajal research program (RyC2019-028414-I). L.L.Y. thank the China Scholarship Council for scholarship support. This project was also supported by the special innovation project fund from the Institute of Wenzhou, Zhejiang University (No. XMGL-KJZX-202204).

REFERENCES

(1) Acar, C.; Dincer, I.; Naterer, G. F. Review of Photocatalytic Water-splitting Methods for Sustainable Hydrogen Production. *Int. J. Energy Res.* **2016**, 40 (11), 1449–1473.

(2) Chen, J.; Qiu, F.; Xu, W.; Cao, S.; Zhu, H. Recent Progress in Enhancing Photocatalytic Efficiency of TiO_2-Based Materials. *Appl. Catal. A: Gen.* **2015**, *495*, 131–140.

(3) Fujishima, A.; Honda, K. Electrochemical Photolysis of Water at a Semiconductor Electrode. *Nature* **1972**, *238* (5358), 37–38.

(4) Jiang, Y.; Ning, H.; Tian, C.; Jiang, B.; Li, Q.; Yan, H.; Zhang, X.; Wang, J.; Jing, L.; Fu, H. Single-Crystal TiO_2 Nanorods Assembly for Efficient and Stable Cocatalyst-Free Photocatalytic Hydrogen Evolution. *Appl. Catal. B: Environ.* **2018**, *229*, 1–7.

(5) O'regan, B.; Grätzel, M. A Low-Cost, High-Efficiency Solar Cell Based on Dye-Sensitized Colloidal TiO_2 Films. *Nature* **1991**, *353* (6346), 737–740.

(6) Nazeeruddin, M. K.; Pechy, P.; Renouard, T.; Zakeeruddin, S. M.; Humphry-Baker, R.; Comte, P.; Liska, P.; Cevey, L.; Costa, E.; Shklover, V. Engineering of Efficient Panchromatic Sensitizers for Nanocrystalline TiO_2-Based Solar Cells. *J. Am. Chem. Soc.* **2001**, *123* (8), 1613–1624.

(7) Hoffmann, M. R.; Martin, S. T.; Choi, W.; Bahnemann, D. W. Environmental Applications of Semiconductor Photocatalysis. *Chem. Rev.* **1995**, *95* (1), 69–96.

(8) Zhang, S.; Cao, S.; Zhang, T.; Lee, J. Y. Plasmonic Oxygen-deficient TiO_{2-x} Nanocrystals for Dual-band Electrochromic Smart Windows with Efficient Energy Recycling. *Adv. Mater.* **2020**, *32* (43), 2004686.

(9) Fox, M. A.; Dulay, M. T. Heterogeneous Photocatalysis. *Chem. Rev.* **1993**, *93* (1), 341–357.

(10) Hernández-Alonso, M. D.; García-Rodríguez, S.; Suárez, S.; Portela, R.; Sánchez, B.; Coronado, J. M. Highly Selective One-Dimensional TiO_2-Based Nanostructures for Air Treatment Applications. *Appl. Catal. B: Environ.* **2011**, *110*, 251–259.

(11) Yu, X.; Hua, T.; Liu, X.; Yan, Z.; Xu, P.; Du, P. Nickel-Based Thin Film on Multiwalled Carbon Nanotubes as an Efficient Bifunctional Electrocatalyst for Water Splitting. *ACS Appl. Mater. Interfaces* **2014**, *6* (17), 15395–15402.

(12) Tsai, C.-C.; Teng, H. Regulation of the Physical Characteristics of Titania Nanotube Aggregates Synthesized from Hydrothermal Treatment. *Chem. Mater.* **2004**, *16* (22), 4352–4358.

(13) Wang, M.; Zhang, F.; Zhu, X.; Qi, Z.; Hong, B.; Ding, J.; Bao, J.; Sun, S.; Gao, C. DRIFTS Evidence for Facet-Dependent Adsorption of Gaseous Toluene on TiO_2 with Relative Photocatalytic Properties. *Langmuir* **2015**, *31* (5), 1730–1736.

(14) Menzel, R.; Duerrbeck, A.; Liberti, E.; Yau, H. C.; McComb, D.; Shaffer, M. S. P. Determining the Morphology and Photocatalytic Activity of Two-Dimensional Anatase Nanoplatelets Using Reagent Stoichiometry. *Chem. Mater.* **2013**, *25* (10), 2137–2145.

(15) Liang, L.; Li, K.; Lv, K.; Ho, W.; Duan, Y. Highly Photoreactive TiO_2 Hollow Microspheres with Super Thermal Stability for Acetone Oxidation. *Chinese J. Catal.* **2017**, *38* (12), 2085–2093.

(16) Yu, J. G.; Su, Y. R.; Cheng, B. Template-free Fabrication and Enhanced Photocatalytic Activity of Hierarchical Macro-/Mesoporous Titania. *Adv. Funct. Mater.* **2007**, *17* (12), 1984–1990.

(17) Yu, J.; Su, Y.; Cheng, B.; Zhou, M. Effects of PH on the Microstructures and Photocatalytic Activity of Mesoporous Nanocrystalline Titania Powders Prepared via Hydrothermal Method. *J. Mol. Catal. A Chem.* **2006**, *258* (1–2), 104–112.

(18) Tian, J.; Zhao, Z.; Kumar, A.; Boughton, R. I.; Liu, H. Recent Progress in Design, Synthesis, and Applications of One-Dimensional TiO_2 Nanostructured Surface Heterostructures: A Review. *Chem. Soc. Rev.* **2014**, *43* (20), 6920–6937.

(19) Pepin, P. A.; Lee, J. D.; Murray, C. B.; Vohs, J. M. Thermal and Photocatalytic Reactions of Methanol and Acetaldehyde on Pt-Modified Brookite TiO_2 Nanorods. *ACS Catal.* **2018**, *8* (12), 11834–11846.

(20) Pradhan, S. K.; Reucroft, P. J.; Yang, F.; Dozier, A. Growth of TiO_2 Nanorods by Metalorganic Chemical Vapor Deposition. *J. Cryst. Growth* **2003**, *256* (1–2), 83–88.

(21) Yang, H. G.; Zeng, H. C. Preparation of Hollow Anatase TiO_2 Nanospheres via Ostwald Ripening. *J. Phys. Chem.* **2004**, *108* (11), 3492–3495.

(22) Alotaibi, A. M.; Sathasivam, S.; Williamson, B. A. D.; Kafizas, A.; Sotelo-Vazquez, C.; Taylor, A.; Scanlon, D. O.; Parkin, I. P. Chemical Vapor Deposition of Photocatalytically Active Pure Brookite TiO_2 Thin Films. *Chem. Mater.* **2018**, *30* (4), 1353–1361.

(23) Nian, J.-N.; Teng, H. Hydrothermal Synthesis of Single-Crystalline Anatase TiO_2 Nanorods with Nanotubes as the Precursor. *J. Phys. Chem. B* **2006**, *110* (9), 4193–4198.

(24) Liu, B.; Aydil, E. S. Growth of Oriented Single-Crystalline Rutile TiO_2 Nanorods on Transparent Conducting Substrates for Dye-Sensitized Solar Cells. *J. Am. Chem. Soc.* **2009**, *131* (11), 3985–3990.

(25) Yu, Y.; Xu, D. Single-Crystalline TiO_2 Nanorods: Highly Active and Easily Recycled Photocatalysts. *Appl. Catal. B: Environ.* **2007**, *73* (1–2), 166–171.

(26) Yang, Z.; Wang, B.; Cui, H.; An, H.; Pan, Y.; Zhai, J. Synthesis of Crystal-Controlled TiO_2 Nanorods by a Hydrothermal Method: Rutile and Brookite as Highly Active Photocatalysts. *J. Phys. Chem. C* **2015**, *119* (29), 16905–16912.

(27) Naicker, P. K.; Cummings, P. T.; Zhang, H.; Banfield, J. F. Characterization of Titanium Dioxide Nanoparticles Using Molecular Dynamics Simulations. *J. Phys. Chem. B* **2005**, *109* (32), 15243–15249.

(28) Gordon, T. R.; Cargnello, M.; Paik, T.; Mangolini, F.; Weber, R. T.; Fornasiero, P.; Murray, C. B. Nonaqueous Synthesis of TiO_2 Nanocrystals Using TiF_4 to Engineer Morphology, Oxygen Vacancy Concentration, and Photocatalytic Activity. *J. Am. Chem. Soc.* **2012**, *134* (15), 6751–6761.

(29) Zhang, Z.; Zhong, X.; Liu, S.; Li, D.; Han, M. Aminolysis Route to Monodisperse Titania Nanorods with Tunable Aspect Ratio. *Angew. Chem. Int. Ed.* **2005**, *44* (22), 3466–3470.

(30) Biswas, A.; Chakraborty, A.; Jana, N. R. Nitrogen and Fluorine Codoped, Colloidal TiO_2 Nanoparticle: Tunable Doping, Large Red-Shifted Band Edge, Visible Light Induced Photocatalysis, and Cell Death. *ACS Appl. Mater. Interfaces* **2017**, *10* (2), 1976–1986.

(31) Zhang, Z.; Wu, Q.; Johnson, G.; Ye, Y.; Li, X.; Li, N.; Cui, M.; Lee, J. D.; Liu, C.; Zhao, S. Generalized Synthetic Strategy for Transition-Metal-Doped Brookite-Phase TiO_2 Nanorods. *J. Am. Chem. Soc.* **2019**, *141* (42), 16548–16552.

(32) Xiong, C.; Deng, X.; Li, J. Preparation and Photodegradation Activity of High Aspect Ratio Rutile TiO_2 Single Crystal Nanorods. *Appl. Catal. B: Environ.* **2010**, *94* (3–4), 234–240.

(33) Murakami, N.; Katayama, S.; Nakamura, M.; Tsubota, T.; Ohno, T. Dependence of Photocatalytic Activity on Aspect Ratio of Shape-Controlled Rutile Titanium (IV) Oxide Nanorods. *J. Phys. Chem. C* **2011**, *115* (2), 419–424.

(34) Cozzoli, P. D.; Kornowski, A.; Weller, H. Low-Temperature Synthesis of Soluble and Processable Organic-Capped Anatase TiO_2 Nanorods. *J. Am. Chem. Soc.* **2003**, *125* (47), 14539–14548.

(35) Yun, H. J.; Lee, H.; Joo, J. B.; Kim, W.; Yi, J. Influence of Aspect Ratio of TiO_2 Nanorods on the Photocatalytic Decomposition of Formic Acid. *J. Phys. Chem. C* **2009**, *113* (8), 3050–3055.

(36) An, G. W.; Mahadik, M. A.; Chae, W.-S.; Kim, H. G.; Cho, M.; Jang, J. S. Enhanced Solar Photoelectrochemical Conversion Efficiency of the Hydrothermally-Deposited TiO_2 Nanorod Arrays: Effects of the Light Trapping and Optimum Charge Transfer. *Appl. Surf. Sci.* **2018**, *440*, 688–699.

(37) Ohno, T.; Higo, T.; Saito, H.; Yuajn, S.; Jin, Z.; Yang, Y.; Tsubota, T. Dependence of Photocatalytic Activity on Aspect Ratio of a Brookite TiO_2 Nanorod and Drastic Improvement

in Visible Light Responsibility of a Brookite TiO_2 Nanorod by Site-Selective Modification of Fe^{3+} on Exposed Faces. *J. Mol. Catal. A Chem.* **2015**, *396*, 261–267.

(38) Fu, B.; Wu, Z.; Cao, S.; Guo, K.; Piao, L. Effect of Aspect Ratios of Rutile TiO_2 Nanorods on Overall Photocatalytic Water Splitting Performance. *Nanoscale* **2020**, *12* (8), 4895–4902.

(39) Cargnello, M.; Montini, T.; Smolin, S. Y.; Priebe, J. B.; Delgado Jaén, J. J.; Doan-Nguyen, V. V. T.; McKay, I. S.; Schwalbe, J. A.; Pohl, M.-M.; Gordon, T. R. Engineering Titania Nanostructure to Tune and Improve Its Photocatalytic Activity. *Proc. Natl. Acad. Sci. U. S. A.* **2016**, *113* (15), 3966–3971.

(40) Amano, F.; Prieto-Mahaney, O.-O.; Terada, Y.; Yasumoto, T.; Shibayama, T.; Ohtani, B. Decahedral Single-Crystalline Particles of Anatase Titanium (IV) Oxide with High Photocatalytic Activity. *Chem. Mater.* **2009**, *21* (13), 2601–2603.

(41) Randorn, C.; Irvine, J. T. S. Synthesis and Visible Light Photoactivity of a High Temperature Stable Yellow TiO_2 Photocatalyst. *J. Mater. Chem.* **2010**, *20* (39), 8700–8704.

(42) Naldoni, A.; D'Arienzo, M.; Altomare, M.; Marelli, M.; Scotti, R.; Morazzoni, F.; Selli, E.; Dal Santo, V. Pt and Au/TiO_2 Photocatalysts for Methanol Reforming: Role of Metal Nanoparticles in Tuning Charge Trapping Properties and Photoefficiency. *Appl. Catal. B: Environ.* **2013**, *130*, 239–248.

(43) Hoang, S.; Berglund, S. P.; Hahn, N. T.; Bard, A. J.; Mullins, C. B. Enhancing Visible Light Photo-Oxidation of Water with TiO_2 Nanowire Arrays via Cotreatment with H_2 and NH_3: Synergistic Effects between Ti^{3+} and N. *J. Am. Chem. Soc.* **2012**, *134* (8), 3659–3662.

(44) Grabstanowicz, L. R.; Gao, S.; Li, T.; Rickard, R. M.; Rajh, T.; Liu, D.-J.; Xu, T. Facile Oxidative Conversion of TiH_2 to High-Concentration Ti^{3+}-Self-Doped Rutile TiO_2 with Visible-Light Photoactivity. *Inorg. Chem.* **2013**, *52* (7), 3884–3890.

(45) Guillemot, F.; Porté, M. C.; Labrugère, C.; Baquey, C. Ti^{4+} to Ti^{3+} Conversion of TiO_2 Uppermost Layer by Low-Temperature Vacuum Annealing: Interest for Titanium Biomedical Applications. *J. Colloid. Interface Sci.* **2002**, *255* (1), 75–78.

(46) Lu, C.; Ma, Y.; Cao, Y.; Huang, Q.; Wang, J. Fluorine Doping-Induced Oxygen Vacancy-Rich TiO_2 via Contact Activation for Signal Boosting in Electrochemical Sensing. *Chem. Eng. J.* **2023**, *468*, 143598.

(47) Yu, J. C.; Zhang, L.; Yu, J. Direct Sonochemical Preparation and Characterization of Highly Active Mesoporous TiO_2 with a Bicrystalline Framework. *Chem. Mater.* **2002**, *14* (11), 4647–4653.

(48) Zhang, J.; Lei, Y.; Cao, S.; Hu, W.; Piao, L.; Chen, X. Photocatalytic Hydrogen Production from Seawater under Full Solar Spectrum without Sacrificial Reagents Using TiO_2 Nanoparticles. *Nano Res.* **2022**, *15* (3), 2013–2022.

(49) Cao, S.; Sui, N.; Zhang, P.; Zhou, T.; Tu, J.; Zhang, T. TiO_2 Nanostructures with Different Crystal Phases for Sensitive Acetone Gas Sensors. *J. Colloid. Interface Sci.* **2022**, *607*, 357–366.

(50) Puga, A. V. Photocatalytic Production of Hydrogen from Biomass-Derived Feedstocks. *Coord. Chem. Rev.* **2016**, *315*, 1–66.

(51) Xing, C.; Zhang, Y.; Liu, Y.; Wang, X.; Li, J.; Martínez-Alanis, P. R.; Spadaro, M. C.; Guardia, P.; Arbiol, J.; Llorca, J. Photodehydrogenation of Ethanol over Cu_2O/TiO_2 Heterostructures. *Nanomaterials* **2021**, *11* (6), 1399.

(52) Kitano, M.; Hara, M. Heterogeneous Photocatalytic Cleavage of Water. *J. Mater. Chem.* **2010**, *20* (4), 627–641.

(53) Castedo, A.; Casanovas, A.; Angurell, I.; Soler, L.; Llorca, J. Effect of Temperature on the Gas-Phase Photocatalytic H_2 Generation Using Microreactors under UVA and Sunlight Irradiation. *Fuel* **2018**, *222*, 327–333.

(54) Zhang, J.; Ma, X.; Zhang, L.; Lu, Z.; Zhang, E.; Wang, H.; Kong, Z.; Xi, J.; Ji, Z. Constructing a Novel n–p–n Dual Heterojunction between Anatase TiO_2 Nanosheets with Co-exposed {101},{001} Facets and Porous ZnS for Enhancing Photocatalytic Activity. *J. Phys. Chem. C* **2017**, *121* (11), 6133–6140.

(55) Liu, S.; Wu, J.; Liu, X.; Jiang, R. $TiO_2/V–TiO_2$ Composite Photocatalysts with an n–n Heterojunction Semiconductor Structure. *J. Mol. Catal. A Chem.* **2010**, *332* (1–2), 84–92.

(56) Wang, X.; Xia, R.; Muhire, E.; Jiang, S.; Huo, X.; Gao, M. Highly Enhanced Photocatalytic Performance of TiO_2 Nanosheets through Constructing TiO_2/TiO_2 Quantum Dots Homojunction. *Appl. Surf. Sci.* **2018**, *459*, 9–15.

(57) Laidler, K. J. The Development of the Arrhenius Equation. *J. Chem. Educ.* **1984**, *61* (6), 494.

(58) Wardman, P. Reduction Potentials of One-electron Couples Involving Free Radicals in Aqueous Solution. *J. Phys. Chem. Ref. Data* **1989**, 18 (4), 1637–1755.

Graphic for manuscript